



HAL
open science

Frictional weakening leads to unconventional singularities during dynamic rupture propagation

F. Paglialunga, F. Passelègue, M. Lebihain, M. Violay

► **To cite this version:**

F. Paglialunga, F. Passelègue, M. Lebihain, M. Violay. Frictional weakening leads to unconventional singularities during dynamic rupture propagation. *Earth and Planetary Science Letters*, 2024, 626, pp.118550. 10.1016/j.epsl.2023.118550 . hal-04373465

HAL Id: hal-04373465

<https://hal.science/hal-04373465>

Submitted on 5 Jan 2024

HAL is a multi-disciplinary open access archive for the deposit and dissemination of scientific research documents, whether they are published or not. The documents may come from teaching and research institutions in France or abroad, or from public or private research centers.

L'archive ouverte pluridisciplinaire **HAL**, est destinée au dépôt et à la diffusion de documents scientifiques de niveau recherche, publiés ou non, émanant des établissements d'enseignement et de recherche français ou étrangers, des laboratoires publics ou privés.



Distributed under a Creative Commons Attribution 4.0 International License

Frictional weakening leads to unconventional singularities during dynamic rupture propagation

F. Paglialunga^a, F. Passelègue^b, M. Lebihain^c, M. Violay^a

^a*LEMR, École Polytechnique Fédérale de Lausanne, Lausanne, Switzerland*

^b*Géoazur, ESEILA, Université Côte d'Azur, CNRS, Observatoire de la Côte d'Azur, IRD, Sophia Antipolis, France., Nice, France*

^c*Navier, Ecole des Ponts, Univ Gustave Eiffel, CNRS, Marne-la-Vallée, France*

Abstract

Earthquakes i.e. frictional ruptures, are commonly described by singular solutions of shear crack motions. These solutions assume a square root singularity order around the rupture tip and a constant shear stress value behind it, implying scale-independent edge-localized energy. However, recent observations of large-scale thermal weakening accompanied by decreasing shear stress potentially affecting the singularity order can challenge this assumption. In this study, we replicate earthquakes in a laboratory setting by conducting stick-slip experiments on PMMA samples under normal stress ranging from 1 to 4 MPa. Strain gauges rosettes, located near the frictional interface, are used to analyze each rupture event, enabling the investigation of shear stress evolution, slip velocity, and material displacement as a function of distance from the rupture tip. Our analysis of the rupture dynamics provides compelling experimental evidence of frictional rupture driven by enhanced thermal weakening. The observed rupture fronts exhibit unconventional singularity orders and display slip-dependent breakdown work (on-fault dissipated energy). Moreover, these findings elucidate the challenges associated

21 with *a priori* estimating the energy budget controlling the velocity and fi-
22 nal extent of a seismic rupture, when thermal weakening is activated during
23 seismic slip.

24 **1. Introduction**

25 Frictional rupture phenomena, including natural earthquakes, are often
26 described by singular solutions of shear crack motions (Freund, 1979; Palmer
27 and Rice, 1973; Rice, 1980). For such cracks, the stress field at the rupture
28 tip is described by a square root singularity ($\xi = -0.5$), constant residual
29 stress is expected far behind the rupture tip, and the energy balance condi-
30 tion equates the energy release rate G (i.e. rupture growth driving force) to
31 a constant value of fracture energy G_c (i.e. resistance to rupture growth).
32 This was confirmed by experimental and numerical observations, where the
33 onset of frictional sliding, the evolution of the rupture speed, and the rupture
34 length were predicted by Linear Elastic Fracture Mechanics (LEFM) (Bayart
35 et al., 2016; Kammer et al., 2015; Kammer and McLaskey, 2019; Svetlizky
36 and Fineberg, 2014; Xu et al., 2019), and suggesting that the fracture energy
37 controlling the dynamics of the rupture tip might be an interface property.
38 Such an analysis often relies on the hypothesis of negligible frictional weak-
39 ening far away from the rupture tip (i.e. outside of the cohesive zone).

40 However, it is widely recognized that fault shear stress is likely to evolve
41 during seismic slip due to (i) velocity and slip dependencies (Marone, 1998),
42 (ii) activation of thermal weakening processes (Di Toro et al., 2011; Hi-
43 rose and Shimamoto, 2005; Rice, 2006), (iii) dilatancy inducing fluid pres-
44 sure changes (Brantut, 2020; Rice and Rudnicki, 1979; Segall et al., 2010).

45 These changes in the residual stress behind the rupture tip could induce a
46 slip dependency of the apparent fracture energy (nowadays more commonly
47 called breakdown work (Tinti et al., 2005)) estimated for natural earthquakes
48 (Abercrombie and Rice, 2005; Lambert and Lapusta, 2020), in contrast to
49 the LEFM definition. The breakdown work W_{bd} is a quantity commonly
50 used to study the energy balance of earthquakes and is defined as an energy
51 term including all on-fault dissipative processes $W_{\text{bd}} = \int_0^D \tau(D') - \tau_{\text{min}} dD'$,
52 with τ the shear stress acting on the fault, τ_{min} the minimum shear stress
53 reached on-fault, and D the fault slip. It can be observed that, by defi-
54 nition, W_{bd} is a slip-dependent quantity. It is therefore important to be
55 aware of how possible stress weakening may affect rupture dynamics and
56 the energy release that controls it. Such weakening phenomenon has been
57 observed in high-velocity friction experiments (for a comprehensive review,
58 see (Di Toro et al., 2011)). Nonetheless, friction experiments seldom exhibit
59 elastodynamic rupture propagation due to the imposed fault slip by the ex-
60 perimental procedure (Chen et al., 2021). Consequently, the experimental
61 documentation of the coupling between fault weakening and elastodynamic
62 rupture response remains limited (Rosakis et al., 2020; Paglialunga et al.,
63 2022).

64 In these regards, our recent work highlighted that a long-tailed weakening
65 can emerge after a first rapid weakening during frictional rupture experiments
66 (Paglialunga et al., 2022), resulting in a slip-dependent breakdown work.
67 Despite this observation, the rupture dynamics, analyzed through LEFM,
68 showed to be controlled by a constant fracture energy G_c , in agreement with
69 previous studies (Bayart et al., 2016; Kammer et al., 2015; Kammer and

70 McLaskey, 2019; Svetlizky and Fineberg, 2014; Xu et al., 2019). However,
 71 analyzing such frictional ruptures in the framework of LEFM relies on the
 72 assumption of constant residual stress behind the rupture tip. The observed
 73 long-tailed weakening could call into question this assumption and limit the
 74 framework’s applicability to fully describe frictional ruptures, explaining the
 75 observed mismatch between G_c and W_{bd} (Paglialunga et al., 2022).

76 Moreover, theoretical studies have shown that continuous stress weaken-
 77 ing can modify the singularity order controlling the stress and displacement
 78 fields around the rupture tip, deviating from the square-root singularity com-
 79 monly adopted in LEFM, and leading to an unconventional singularity order
 80 ($\xi \neq -0.5$) (Garagash et al., 2011; Viesca and Garagash, 2015; Brantut
 81 and Viesca, 2017; Brener and Bouchbinder, 2021b). In particular, when
 82 frictional ruptures are described by $\xi \neq -0.5$, the stress σ_{ij} and displace-
 83 ment u_i fields obey respectively the following scaling relationships (Brener
 84 and Bouchbinder, 2021a): $\sigma_{ij} \propto K^{(\xi)} r^\xi$ and $u_i \propto K^{(\xi)} r^{(\xi+1)}/\mu$, with $K^{(\xi)}$
 85 the ξ - generalized dynamic stress intensity factor, $r = x - x_{\text{tip}}$ the distance
 86 from the rupture tip of a point of observation located on the fault plane,
 87 and μ the dynamic shear modulus. These lead to the following relation:
 88 $W_{\text{bd}} \propto [K^{(\xi)}]^2 r^{(1+2\xi)}/\mu$, valid for $r > x_c$, with x_c the cohesive zone size
 89 (Eq. (5) from (Brener and Bouchbinder, 2021a)). From this relation, it can
 90 be easily noticed that for $\xi = -0.5$, the W_{bd} dependence on r completely
 91 vanishes, making the breakdown work independent of the distance from the
 92 rupture tip. This does not happen when $\xi \neq -0.5$, for which W_{bd} has a
 93 direct dependence on r .

94 So far, the occurrence of such unconventional singularities during fric-

95 tional ruptures has not been measured at the laboratory scale. In this pa-
96 per, we present new data analyzed in a recently-derived theoretical frame-
97 work, demonstrating the first experimental evidence of strain and stress per-
98 turbation caused by unconventional singularities associated with velocity-
99 dependent frictional weakening. These experimental findings are supported
100 by theoretical explanations about the emergence of unconventional singular
101 fields during dynamic rupture.

102 **2. Methods**

103 We performed stick-slip experiments in a biaxial apparatus working in a
104 2D single shear configuration under an applied normal stress ranging from
105 1 to 4 MPa (Figure 1a). The experimental setup is the same one used and
106 described in (Paglialunga et al., 2022). The tested samples consist of two
107 polymethylmethacrylate (PMMA) blocks of dimensions (20x10x3) cm (top
108 block) and (50x10x3) cm (bottom block), generating, once put into contact,
109 an artificial fault of (20x3) cm. The external loading is imposed using two
110 hydraulic pumps. The normal load is applied to the top block and kept
111 constant while the shear load is manually increased and applied to the bottom
112 block inducing, once reached the fault strength, stick-slip events. Strain
113 gages rosettes (oriented along 45° , 90° , 135° to the fault plane), located 1 mm
114 away from the frictional interface, were used to compute the local strain and
115 stress tensors. Note that at such distance from the fault plane, the dynamic
116 propagation of the rupture will induce a stress perturbation (rise of stress
117 ahead of the rupture tip, followed by a stress drop behind it). Such a stress
118 perturbation will be maximum on the fault plane ($y = 0+$) and decrease

119 away from it ($y > 0$), as predicted by fracture mechanics. This feature is
 120 not observable through macroscopic measurements of strain or stress, hence
 121 the need for local ones. The strain tensor rotation was obtained through the
 122 conversion of $\varepsilon_1, \varepsilon_2, \varepsilon_3$ into $\varepsilon_{xx}, \varepsilon_{xy}, \varepsilon_{yy}$ following:

$$\varepsilon_{xy} = \frac{\varepsilon_3 - \varepsilon_2}{2}, \quad (1)$$

$$\varepsilon_{yy} = \varepsilon_1, \quad (2)$$

$$\varepsilon_{xx} = \varepsilon_3 + \varepsilon_2 - \varepsilon_1 \quad (3)$$

125 The local strain temporal evolution shows clear perturbations concurrent
 126 with stick-slips (Figure 1b). By zooming-in in time, details of the instability
 127 can be caught (Figure 1c), showing a first (main) rupture front, followed by a
 128 series of secondary fronts probably caused by rupture reflections at the fault
 129 edges. To study the rupture dynamics, only the main front was considered,
 130 selecting a time window around the first strain perturbation (Figure 1d-e).
 131 Together with the vicinity of the measurement location to the fault, the
 132 measuring interval is of paramount importance for properly addressing the
 133 elastodynamics of the studied events. From here the need for a sufficiently
 134 high recording frequency (2 MHz in this case) and a well-defined and short
 135 time interval excluding possible subsequent events. Note that the following
 136 analysis and discussions will exclusively focus on the dynamics of the main
 137 rupture front for each stick-slip event. All the experimental curves that will
 138 be shown will refer to a defined time window, systematically smaller than the
 139 expected propagation time along the fault interface (for example, the rupture
 140 showed in Figure 1e is described by a temporal window of $\sim 45 \mu s$). The rup-
 141 ture propagation velocity C_f was estimated by computing the ratio between

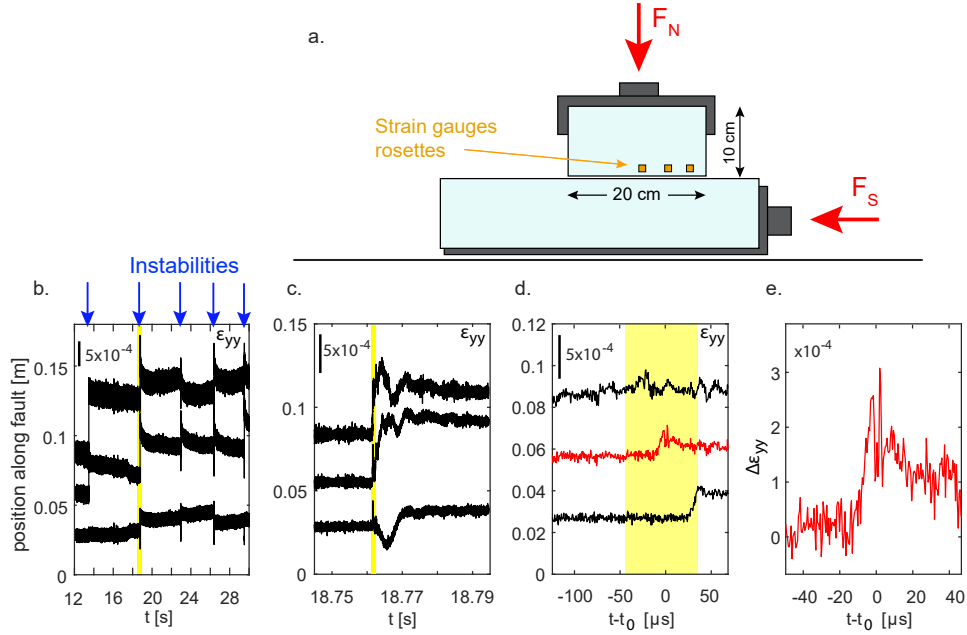


Figure 1: a. Experimental setup - Direct shear biaxial apparatus with PMMA samples generating an artificial fault. Strain gauges rosettes are located along the fault at a distance of 1-1.5 mm from the fault plane. b. Temporal evolution of vertical strain (obtained through high-frequency strain gauges acquisition system) at the three different locations along the fault. When the fault experiences instability, the shear rupture propagates along the interface and causes a strain perturbation concurrent with the passage of the front (indicated by the blue arrows). Yellow shaded areas indicate the time window selection shown in the following panel. c. Zoom-in of (b). d. Zoom-in of (.c) The red curve indicates the strain gauge location shown in panel (e). e. Vertical strain temporal evolution for the central location. Please note that the y-axis and x-axis limits change for each panel. t_0 refers to the arrival time of the rupture for the central strain gauge.

142 the distance among the strain gauge locations and the rupture front travel
143 time from one location to the other. For each event, the particle velocity was
144 then computed through the strain component parallel to the slip direction
145 as $\dot{u}_x = -C_f \varepsilon_{xx}$. This estimate has been shown to be comparable to distinct
146 measurements of slip motions associated with the propagation of the seis-
147 mic rupture in previous experimental studies (Svetlizky and Fineberg, 2014;
148 Paglialunga et al., 2022). The fault slip velocity was considered equal to twice
149 the particle velocity measured through the strain gauges ($V = 2\dot{u}_x$), assum-
150 ing an anti-symmetrical distribution of slip and slip rate. This assumption
151 seems legitimate given that the two samples have comparable dimensions,
152 the same width, and are made of the same material. Integrating V during
153 the propagation time, local horizontal displacement u_x could be estimated as
154 well. The slip displacement D of the fault is computed as twice (refer to the
155 assumption described just above) the horizontal displacement ($D = 2u_x$),
156 assuming the material displacement measured through the strain gauge 1
157 mm away from the fault is comparable to the one occurring on-fault. The
158 acquired temporal evolutions of strain were converted into spatial evolutions
159 following the methods used in Svetlizky and Fineberg (2014), and by assum-
160 ing that the rupture velocity obtained was locally constant during rupture
161 propagation. Moreover, by assuming plane stress conditions, the stress tensor
162 was computed through the elastic properties of PMMA. Given the viscoelas-
163 tic nature of PMMA, dynamic values of its elastic modulus were used in this
164 study, $E = 5.7$ GPa, and a Poisson ratio $\nu = 0.33$, both obtained through
165 bench measurements of seismic velocities ($C_P = 2705$ m/s and $C_S = 1340$
166 m/s).

167 **3. Results**

168 Each rupture event was studied through the evolution of shear stress, slip
 169 velocity, and material displacement as a function of the distance from the
 170 rupture tip (Fig. 2). In such spontaneous ruptures, the slip (or slip rate)
 171 history results from the coupling of elastodynamics and the constitutive fric-
 172 tion law, rather than being prescribed. In all the studied events, local shear
 173 stress evolution exhibited an increase ahead of the rupture tip followed by
 174 a first significant decrease within the first micrometers of slip and a second
 175 mild one within larger distances (Fig. 2a) as recently observed (Paglialunga
 176 et al., 2022). A rapid increase of slip velocity was observed concurrent with
 177 the passage of the rupture front, followed by a slow decay occurring with
 178 distance from the rupture tip. The peak slip velocity V_{\max} showed a clear
 179 dependence with estimated rupture speed, with ~ 0.08 m/s for $C_f \approx 220$
 180 m/s up to ~ 0.8 m/s for $C_f \approx 840$ m/s (Fig. 2b). The evolution of horizon-
 181 tal displacement u_x presented values close to $0\mu m$ ahead of the rupture tip
 182 (values slightly deviate from 0 due to off-fault measurement) and a sharp in-
 183 crease behind it (Fig. 2c), with final displacements ranging between 3.9 and
 184 $28 \mu m$. Subsequently, the fault strength weakening was analyzed through
 185 the evolution of the local shear stress τ with the fault's slip displacement
 186 D . The fault's weakening presents a sharp decrease of shear stress occur-
 187 ring within the first microns of slip, followed by a milder decrease occurring
 188 within a larger amount of slip (Fig. 3a). The breakdown work evolution was
 189 computed as

$$W_{\text{bd}} = \int_{D((x-x_{\text{tip}})=0)}^D (\tau - \tau(D)) dD \quad (4)$$

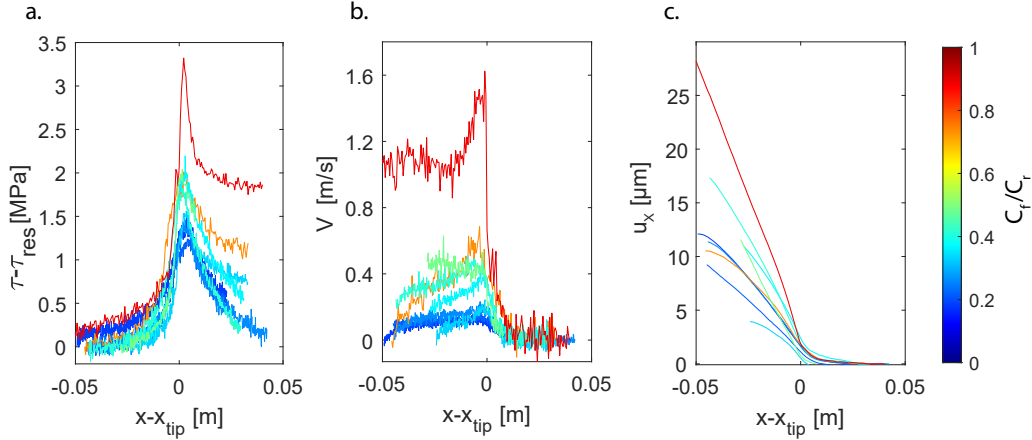


Figure 2: Elastic fields around the rupture tip. Evolution of a. shear stress computed from the measured shear strain ε_{xy} , b. slip velocity computed from the measured horizontal strain ε_{xx} , and c. material displacement computed from the estimated slip velocity for several events presenting different C_f (colorbar).

190 where $D((x - x_{\text{tip}}) = 0)$ is the displacement at the passage of the rupture tip.
 191 Since no slip is expected to occur ahead of the rupture tip on the fault plane
 192 ($C_f = 0$ when $(x - x_{\text{tip}}) > 0$), the breakdown work evolution was computed
 193 only from slip occurring after the passage of the rupture tip ($x - x_{\text{tip}} = 0$),
 194 neglecting fictitious contributions due to elastic strain of the bulk at the
 195 measurement location. The evolution of W_{bd} showed a first increase with
 196 slip described by a slope close to 1 : 2 and a subsequent increase described
 197 by a slope of $\sim 1 : 0.6(\pm 0.1)$ (Fig. 3b), suggesting the existence of anomalous
 198 singularities ($\xi \neq -0.5$). Given our interest in studying the second branch
 199 of this evolution, the slope of it was measured. This was done by fitting
 200 the evolution of W_{bd} with D for $D > D_c$ with a first-degree polynomial in
 201 log-log scale. Then, ξ was derived from estimates of the power law exponent

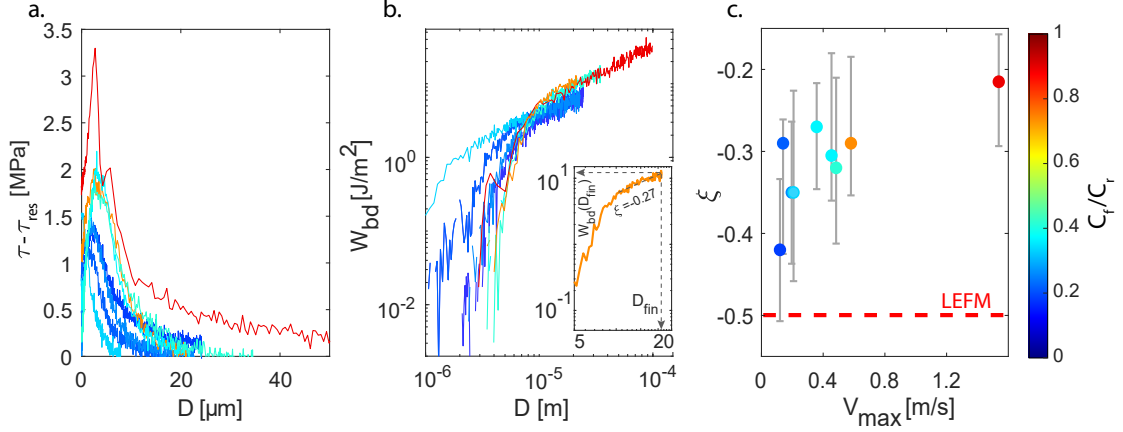


Figure 3: Slip-dependent breakdown work and the emergence of unconventional singularities. a. Evolution of $(\tau - \tau_{\text{res}})$ with D defining the fault’s weakening for different events. The integration of these curves leads to the evolution of W_{bd} with D for different C_f (b). For each curve, the slope of the second branch of the evolution corresponds to a given value of singularity order. c. Evolution of estimated ξ values with peak slip velocity V_{max} .

202 through:

$$W_{\text{bd}}(D) = G_c \left(\frac{D}{D_c} \right)^{\frac{1+2\xi}{1+\xi}}, \quad (5)$$

203 for large slip displacement $D \gtrsim D_c$. The values were found to range between
 204 -0.4 and -0.2 (Fig. 3c). Another possible route proposed by Brener and
 205 Bouchbinder (2021a) is to estimate the deviation $\Delta\xi = \xi + 1/2$ of ξ from
 206 the LEFM value $-1/2$ from the dependence of the breakdown energy in
 207 the distance $r = x - x_{\text{tip}}$ from the crack tip. However, this requires prior
 208 knowledge of the fracture energy G_c and the process zone size x_c , which are
 209 difficult to constrain from experimental measurements.

210 **4. Theoretical modeling of the kinematic fields around the rupture**
211 **tip for unconventional singularity order**

212 While the first increase of breakdown work with slip can be explained by
213 a slip-weakening behavior of the fault, the subsequent increase (power law of
214 1:0.6) is unexpected from the conventional theory of LEFM. If such a con-
215 tinuous weakening stage controlled the dynamics of the rupture, stress fields
216 with a scaling $\sigma \propto r^\xi$ should be observed behind the rupture tip, as expected
217 from theoretical studies (Brantut and Viesca, 2017; Brener and Bouchbinder,
218 2021b; Garagash et al., 2011; Viesca and Garagash, 2015), with the singular-
219 ity order ξ different from the square root singularity. To further investigate
220 the dynamics of rupture, the temporal evolution of the strain perturbations
221 generated by the passage of the rupture front $(\Delta\varepsilon_{xy}, \Delta\varepsilon_{xx})$ was compared
222 to the theoretical predictions obtained considering both a square root singu-
223 larity (LEFM) and an unconventional singularity (Brener and Bouchbinder,
224 2021a).

225 For the LEFM theoretical prediction, the stress field perturbation around
226 the rupture tip takes the following general form (for a detailed description
227 please refer to Freund (1998); Anderson (2017)):

$$\Delta\sigma_{ij}(r, \theta) = \frac{K_{II}}{\sqrt{2\pi r}} \Sigma_{ij}^{II}(\theta, C_f) \quad (6)$$

228 where K_{II} the stress intensity factor, and $\Sigma_{ij}^{II}(\theta, C_f)$ the angular variation
229 function. Coordinates are expressed in the polar system with (r, θ) respec-
230 tively the distance from the crack tip and the angle to the crack's plane.

231 In the unconventional theory framework, the stress fields were derived
232 from the elastodynamic equations assuming a steady-state rupture velocity.

233 The equations obtained present the following form:

$$234 \quad \sigma_{xx}(r, \theta) = \frac{4(\xi + 1)K_{II}^{(\xi)}}{\sqrt{2\pi}R(C_f)} [\alpha_s(1 + 2\alpha_d^2 - \alpha_s^2)r_d^\xi \sin(\xi\theta_d) - \alpha_s(1 + \alpha_s^2)r_s^\xi \sin(\xi\theta_s)], \quad (7)$$

$$235 \quad \tau(r, \theta) = \sigma_{xy}(r, \theta) = \tau_{\min} + \frac{2(\xi + 1)K_{II}^{(\xi)}}{\sqrt{2\pi}R(C_f)} [4\alpha_s\alpha_d r_d^\xi \cos(\xi\theta_d) - (1 + \alpha_s^2)^2 r_s^\xi \cos(\xi\theta_s)], \quad (8)$$

$$236 \quad \sigma_{yy}(r, \theta) = -\frac{4(\xi + 1)\alpha_s(1 + \alpha_s^2)K_{II}^{(\xi)}}{\sqrt{2\pi}R(C_f)} [r_d^\xi \sin(\xi\theta_d) - r_s^\xi \sin(\xi\theta_s)], \quad (9)$$

236 where $K_{II}^{(\xi)} = \lim_{r \rightarrow 0} \left(\frac{(2\sqrt{2\pi})}{(\xi+1)} r^{-\xi} \tau(r, 0^{+-}) \right)$ is the ξ -generalized stress intensity factor, $\alpha_d = 1 - \left(\frac{C_f}{C_d} \right)^2$ and $\alpha_s = 1 - \left(\frac{C_f}{C_s} \right)^2$, where (C_d, C_s) are respectively
 237 the P-wave and S-wave velocity, and $R(C_f) = 4\alpha_d\alpha_s - (1 + \alpha_s^2)^2$ is the Rayleigh
 238 function. (r, θ) are corrected for the distortion induced by the dynamic rupture
 239 velocity C_f , becoming $\theta_d = \arctan(\alpha_d \tan(\theta))$, $\theta_s = \arctan(\alpha_s \tan(\theta))$
 240 and $r_d = r \sqrt{1 - \left(\frac{C_f \sin(\theta)}{C_d} \right)^2}$, $r_s = r \sqrt{1 - \left(\frac{C_f \sin(\theta)}{C_s} \right)^2}$.

241 The displacement field related to the unconventional rupture phenomenon
 242 can be predicted by (Brener and Bouchbinder, 2021a):
 243

$$244 \quad u_x(r, \theta) = \frac{2K_{II}^{(\xi)}}{\mu\sqrt{2\pi}} \left[2\alpha_s r_d^{\xi+1} \sin[(\xi + 1)\theta_d] - \alpha_s(1 + \alpha_s^2)r_s^{\xi+1} \sin[(\xi + 1)\theta_s] \right] \quad (10)$$

$$245 \quad u_y(r, \theta) = \frac{2K_{II}^{(\xi)}}{\mu\sqrt{2\pi}} \left[2\alpha_s\alpha_d r_d^{\xi+1} \cos[(\xi + 1)\theta_d] - (1 + \alpha_s^2)r_s^{\xi+1} \cos[(\xi + 1)\theta_s] \right]. \quad (11)$$

246 The values of ξ used to describe the experimental curves were obtained
 247 through the measured evolution of W_{bd} with D as discussed earlier (Brener
 248 and Bouchbinder, 2021a). The stress intensity factor was computed as (Eq. (5))
 249 from (Brener and Bouchbinder, 2021a): $K_{II}^{(\xi)} = \frac{EW_{bd}(D_{fin})}{(1-\nu^2)f_{II}(C_f)r_{fin}^{(1+2\xi)}}$, with E, ν
 respectively the elastic modulus and Poisson's ratio, and $f_{II}(C_f) = \frac{\alpha_s}{(1-\nu)R(C_f)} \frac{C_f^2}{C_s^2}$

250 the universal function of rupture velocity.

251 **5. Description of strain perturbations with theoretical predictions**

252 We now compare the theoretical predictions to experimental strain and
253 displacement evolution of two different frictional ruptures presenting values
254 of $\xi = -0.32, -0.27$, and final values of W_{bd} of 9.5 and 11 J/m², respectively
255 (Fig. 3b). The values of singularity order were obtained as described in the
256 Results section, by computing the slope of the second branch of the W_{bd} vs
257 D curve and using Eq. 5.

258 The above-mentioned comparison is presented in Fig. 4. Note that for both
259 models, i.e. LEFM and unconventional theory, the predictions of strain fail
260 ahead of the rupture tip. This is explained by the fact that the two models
261 assume a dynamic rupture driven along an infinite fault by a shear stress
262 equal to the residual stress. As such, they overlook any finite-size effects
263 emerging from the finiteness of the specimen size and the distance to the
264 applied boundary conditions. Moreover, please note that the measurement
265 location was chosen to be the closest possible to the fault plane (strain gauges
266 at ~ 1 mm), to capture stress and displacement evolution close to the ones
267 occurring on-fault. However, this choice implies the likelihood of performing
268 measurements within the cohesive zone, expected to be for PMMA around
269 2-5 mm. The cohesive zone (indicated in Fig. 4a-d with the shaded grey area)
270 was excluded when performing the LEFM fits, given that this model assumes
271 conditions of small-scale yielding (dissipation zone small with respect to the
272 other length scales).

273 The experimental data were compared with the predictions of LEFM

274 ($\xi = -0.5$) inverting G_c from the best possible fit. The inversion and the
 275 minimization algorithm employed to obtain the best solution of G_c use si-
 276 multaneously two strain components ($\Delta\varepsilon_{xx}$, $\Delta\varepsilon_{xy}$) following the method de-
 277 scribed in previous studies (Svetlizky and Fineberg, 2014) (Fig. 4). $\Delta\varepsilon_{xx}$ and
 278 $\Delta\varepsilon_{xy}$ are obtained by subtracting the initial strain from ε_{xx} and the residual
 279 strain from ε_{xy} .

280 The best fits output values of G_c slightly different from the values of W_{bd}
 281 estimated through the integration of the slip stress curves. The LEFM pre-
 282 dictions do not deviate excessively from the experimental curves for either
 283 event, showing an acceptable but not accurate description of the strain per-
 284 turbations for $\Delta\varepsilon_{xx}$ and $\Delta\varepsilon_{xy}$ (Fig. 4a-b). A stronger deviation is observed
 285 for $\Delta\varepsilon_{xy}$, particularly in the case of $\xi = -0.27$, independently of the distance
 286 from the rupture tip (Fig. 4b). In the second stage, predictions accounting for
 287 the unconventional model were computed. The values of ξ and W_{bd} measured
 288 as described in the Results section were imposed. The unconventional model
 289 returned, for the two events, satisfactory predictions of the evolution of $\Delta\varepsilon_{xx}$
 290 and $\Delta\varepsilon_{xy}$ (Fig. 4a,b). It can be noted that the greater the deviation from
 291 $\xi = -0.5$, the greater the disparities between LEFM and the unconventional
 292 model (Fig. 4a,b). In addition, the prediction obtained for u_x (Fig. 4c,d) is
 293 close to the experimental evolution in terms of magnitude. However, while
 294 u_x evolution is similar within the first microns, the experimental data deviate
 295 from the theoretical prediction far behind the rupture tip (Fig. 4c,d). The
 296 model returned reasonable predictions of u_x for $\xi=-0.32$, and adequate ones
 297 for $\xi=-0.27$.

298 Finally, we compare the experimental data to both models' theoretical

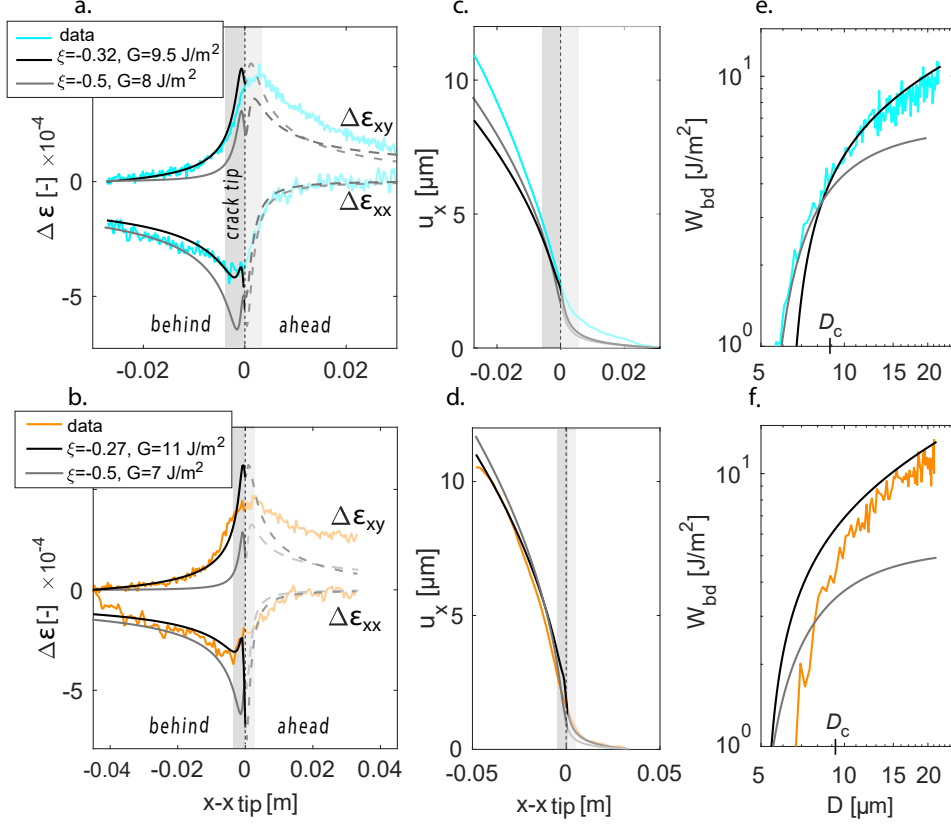


Figure 4: Strain and displacement field described by unconventional singularity for two different events (respectively top and bottom panels). a., b. Comparison of the measured strain perturbations $\Delta\epsilon_{xx}$ and $\Delta\epsilon_{xy}$ with the theoretical predictions considering: i) the estimated unconventional singularities respectively $\xi=-0.32$ (a) and $\xi=-0.27$ (b), and $G = W_{bd}$ (in black) and ii) the LFM conventional singularity $\xi=-0.5$ with $G = G_c$ (the best fit)(in grey). c., d. Evolution of the material displacement u_x with predictions for unconventional and conventional singularity. e., f. Comparison of the experimental evolution of breakdown work with slip estimated at gauge location with theoretical predictions for unconventional theory (black solid line) and LFM (grey solid line).

299 predictions of the evolution of breakdown work with slip behind the crack tip.
300 Starting from the stress evolution estimates computed for both LEFM and
301 unconventional model, the breakdown work was computed following Eq. 4.
302 Please note that neither of the two models is expected to describe the exper-
303 imental evolution for small D , given that both of them rely on a small-scale
304 yielding condition. Concerning the overall evolution, LEFM predictions devi-
305 ate in both quantity and temporal evolution from the experimental data. On
306 the contrary, the unconventional model provides a good prediction, partic-
307 ularly for $D > D_c$, as expected from the unconventional theory (Fig. 4e-f).
308 These results highlight that while LEFM provides reasonable estimates of
309 fracture energy, the unconventional theory provides more coherent predic-
310 tions of breakdown work evolution with slip when enhanced weakening is
311 observed.

312 **6. Flash heating as a possible weakening mechanism**

313 These results provide the first complete evidence of unconventional stress
314 fields during the dynamic propagation of laboratory frictional rupture, caused
315 by continuous stress weakening behind the rupture tip. The observed un-
316 conventional singularity orders could emerge, among others, from frictional
317 weakening mechanisms such as; thermal activation (Bar-sinai et al., 2014),
318 viscous friction (Brener and Marchenko, 2002), powder lubrication (Reches
319 and Lockner, 2010), flash heating (Molinari et al., 1999; Rice, 2006; Brantut
320 and Viesca, 2017), thermal pressurization (Rice, 2006; Viesca and Garagash,
321 2015). Among these, flash heating has been shown to be activated under
322 similar experimental conditions in Homalite (Rubino et al., 2017), and thus

323 could be the best candidate to explain the unconventional stress fields ob-
 324 served in our experiments. Moreover, the high slip rate measured near-fault
 325 promotes the activation of flash heating as previously shown (Molinari et al.,
 326 1999; Rice, 2006; Goldsby and Tullis, 2011). This agrees with the clear de-
 327 pendence of ξ values with maximum slip rate and rupture velocity observed
 328 in our events (Fig. 3c): higher V_{\max} are associated with ξ values that deviate
 329 from the conventional value (-0.5).

330 Flash heating is activated when the fault slip velocity becomes higher
 331 than a critical weakening slip velocity V_w , causing mechanical degradation
 332 of contact asperities during their lifetime (Rice, 2006; Goldsby and Tullis,
 333 2011). The temperature reached at the asperities was computed through
 334 $T_{\text{asp}} = T_{\text{amb}} + \frac{1}{(\rho c_p \sqrt{k\pi})} \tau_c V \sqrt{t_c}$ with T_{amb} the ambient initial temperature,
 335 τ_c the stress acting on the single asperity, t_c the lifetime of a contact, ρ the
 336 bulk density, c_p the bulk specific heat and k the thermal diffusivity. Under
 337 our experimental conditions, the temperature increased with slip velocity, ex-
 338 ceeding the material's melting temperature ($T_{\text{asp}} > T_{\text{melting}} = 160^\circ$) (Fig. 5a,
 339 b), and indicating that melting of asperities probably occurred in our exper-
 340 iments (Rubino et al., 2017). We compared the evolution of W_{bd} with D ,
 341 normalized respectively by G_c and D_c , with asymptotic solutions for flash
 342 heating phenomena (Brantut and Viesca, 2017).

343 For $D < D_c$ (small slip), the evolution of W_{bd} can be described by the
 344 asymptotic solution derived for adiabatic conditions (Brantut and Viesca,
 345 2017):

$$W_{\text{bd}} = \rho c (T_m - T_{\text{amb}}) w \sqrt{2\pi} \left(\frac{D}{V t_w^A + D} \right)^2 \quad (12)$$

346 where $t_w^A = \rho c (T_m - T_f) / \tau_a (\sqrt{2\pi} w) / V_w$ (time required for a layer of thickness

347 $\sqrt{2\pi}w$ to reach T_{melting}), w is the shear zone thickness (assumed here as
348 $w = 4a$ with a the asperity size), and τ_a is a normal stress dependent contact
349 shear stress at the origin of the change in temperature in the fault layer
350 (Fig. 5c). In presence of gouge along the interface, τ_a will correspond to
351 the macroscopic shear stress τ_0 . Along bare rock interfaces, $\tau_a = \tau_c \frac{a}{\Delta L_{\text{asp}}}$,
352 where ΔL_{asp} is the average distance between two asperities (see Annex A for
353 details). Note that this model assumes a constant sliding velocity V . This
354 assumption looks fairly reasonable in our case, as the first part of the stress
355 weakening ($D < D_c$) occurs in a very short time window, during which V is
356 nearly constant.

357 For $D > D_c$, a second asymptotic solution considering the coupled elas-
358 todynamics and frictional motions of the propagating rupture can be used
359 (Brantut and Viesca, 2017):

$$W_{\text{bd}} = \tau_c D_w^{SP} \left(\frac{\mu V_w}{3\pi\tau_a C_f} \right)^{(1/3)} \left(\frac{D}{D_w^{SP}} \right)^{(2/3)} \quad (13)$$

360 where $D_w^{SP} = V_w \alpha \left(\frac{\rho c (T_w - T_f)}{\tau_a V_w} \right)^2$ is a characteristic slip weakening distance.
361 While this asymptotic solution is expected to describe the evolution of break-
362 down work at a larger seismic slip than the one observed in our experiments,
363 this equation can still be used here because (i) heat diffusion at the scale of
364 asperities is expected to control fault weakening when $D > D_c$ and (ii) τ_a
365 increases with τ_0 , through the increase of $\frac{a}{\Delta L_{\text{asp}}}$ with σ_n .

366 Assuming our experimental estimate of C_f , this asymptote well describes the
367 second branch of the evolution of W_{bd} with D (power law with an exponent
368 of 2/3, Fig. 5c). Such scaling is also observed at large slip for thermal pres-
369 surization in drained conditions, suggesting that this exponent is related to

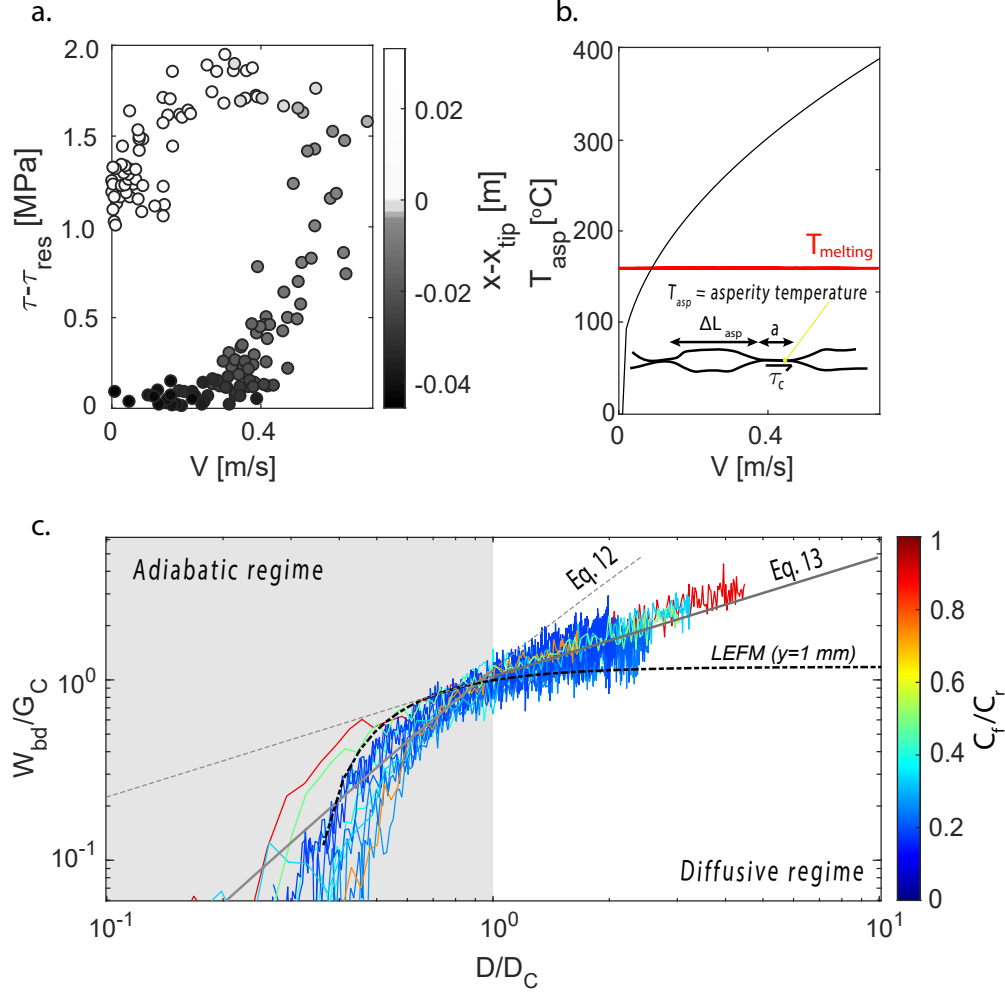


Figure 5: a. Evolution of local shear stress τ , with slip velocity for one event. b. Temperature evolution with slip velocity at asperity scale compared with melting temperature of PMMA ($T_m = 160$). c. Slip dependence of breakdown work (curves are normalized respectively by G_C and D_C). W_{bd} evolution exhibits two power laws with exponents of 2 and 0.6. The experimental curves are all described by the asymptotic solutions related to an adiabatic regime for small D and a diffusive regime for large D (Brantut and Viesca, 2017). The dotted black line shows the expected evolution of W_{bd} assuming LEFM at the strain gauges position.

370 diffusion mechanisms regulating the weakening of faulting during seismic slip
371 (Brantut and Viesca, 2017; Viesca and Garagash, 2015).

372 Importantly, an energy dissipation W_{bd} greater than the fracture energy
373 G_c was already observed in Barras et al. (2020) for sliding interfaces whose
374 frictional behavior is described by a rate-and-state friction law. Despite this
375 excess, the rupture dynamics were well described by a conventional LEFM
376 analysis (with $\xi = -0.5$). This was later justified by Brener and Bouchbinder
377 (2021b), who showed that ruptures along interfaces obeying rate-and-state
378 friction displayed a singularity $\xi = -0.406 \simeq -0.5$, which corresponds to the
379 lower end of our measurements. However, fault characteristics (e.g. rough-
380 ness, fluid diffusivity, etc.) and external factors such as initial stress state
381 or on-fault temperature can alter the friction law that controls interface slip
382 (i.e. flash heating, thermal pressurization, and others) and change the sin-
383 gularity observed near the rupture accordingly. In the case of flash heating,
384 the observed evolution of breakdown work with slip generates, for example,
385 a singularity order $\xi = -0.25$ (Brantut and Viesca, 2017), which corresponds
386 to the higher-end exponents of Fig. 3. In our experiments, continuous val-
387 ues of exponents ξ have been measured between $\xi = -0.42$ (rate-and-state)
388 and $\xi = -0.22$ (flash heating). This can be caused by the presence of a
389 population of contact asperities, each of which have a different size, expe-
390 rience a different normal and shear stress, and reach thus a different value
391 of temperature and slip velocity during rupture (implying that not neces-
392 sarily all contact asperities experience flash heating) resulting, on average,
393 in a smooth transition from rate and state frictional contact for the lower
394 slip velocities (nearly conventional, $\xi = -0.5$) to flash heating for larger slip

395 velocities (unconventional, $\xi = -0.25$).

396 **7. Implications and conclusions**

397 These experimental results show that the continuous weakening activated
398 along the fault can modify the singularity order governing displacement and
399 stress fields around the rupture tip, inducing a slip and scale-dependent
400 breakdown work, rather than a constant one. Moreover, this work high-
401 lights from an experimental point of view that frictional rupture analysis in
402 the linear elastic fracture framework might not always be sufficient when fric-
403 tional weakening mechanisms occur away from the rupture tip. Importantly,
404 as long as the residual stress does not reach a steady-state value far from
405 the rupture tip, as happens for thermal weakening processes, the singular
406 fields will hardly recover the conventional square-root singularity, indepen-
407 dently of the rupture size. One could nonetheless assess the dynamics of
408 such earthquakes, building on a Griffith criterion adapted to unconventional
409 singularities (see Eq. (7) (Brener and Bouchbinder, 2021a)). However, this
410 would involve both the fracture energy and the cohesive zone size that of-
411 ten depends on the structural problem (loading conditions, fault geometry).
412 Furthermore, the activation of thermal mechanisms depends not only on the
413 rupture characteristics such as crack velocity but also on ambient conditions
414 (such as initial temperature) and possibly slip history controlling asperity
415 roughness and strength. As a result, both rupture dynamics and fault weak-
416 ening are expected to be governed by fault geometry and rheology and may
417 vary depending on the natural environment.

418 Our new results highlight the difficulty in *a priori* estimating the relevant

419 parameters governing the dynamics of the seismic rupture, expected to con-
420 trol the final rupture length (earthquake size). One may legitimately wonder
421 whether theoretical models will be able to capture these complex behaviors,
422 or whether numerical simulations, as proposed in recent studies, will be re-
423 quired instead (Lambert and Lapusta, 2020).

424 However, together with the recent development of the unconventional singu-
425 larity theory (Brener and Bouchbinder, 2021a), our results open the door for
426 a better understanding of the rupture dynamics and energy budget of natural
427 earthquakes, through the possible evaluation of the equations of motions for
428 unconventional rupture phenomena.

429 **Appendix A.**

430 For the estimate of ΔL_{asp} , a simplified description of the interface rough-
431 ness is used, considering only one population of asperities of typical size a
432 and height h , separated by an average distance ΔL_{asp} . The number of as-
433 perities was computed considering the following relationship $\frac{A_r}{A_n} = \frac{G_c}{G_{\text{PMMA}}}$
434 (values of G_{PMMA} coming from Marshall et al. (1974)), which lead to $N_{2\text{D}} =$
435 $\frac{G_c}{G_{\text{PMMA}}} \frac{A_n}{\pi D_{\text{asp}}^2/4}$.

436 Assuming an equidistant spacing between the asperities in both direc-
437 tions, the total number of asperities can be written as $N_{2\text{D}} = N_x N_y$ with N_x
438 and N_y respectively the number of rows and columns of asperities located in
439 the x and y directions. The latter numbers are related to the interface dimen-
440 sions through $\frac{N_x}{N_y} = \frac{L_f}{W_f}$, with L_f and W_f respectively the length and width
441 of the interface. Considering this as a 1-D problem, the number of asperities
442 along the interface in the slip direction reads $N_{1\text{D}} = \sqrt{N_{2\text{D}} \frac{L_f}{W_f}}$. The distance
443 between two asperities could then be estimated as $\Delta L_{\text{asp}} = \frac{L_f - N_{1\text{D}} D_{\text{asp}}}{N_{1\text{D}} + 1}$. The
444 contact stress at the origin of the change in temperature of asperities during
445 the seismic slip can be expressed as $\tau_{\text{eff}} = \tau_c \frac{a}{\Delta L_{\text{asp}}}$.

446 **Appendix B.**

447 Acknowledgments.

448 F.P. and M.V. acknowledge support by the European Research Council
449 Starting Grant project 757290-BEFINE.

450 **References**

- 451 Abercrombie, R.E., Rice, J.R., 2005. Can observations of earthquake scaling
452 constrain slip weakening? *Geophysical Journal International* 162, 406–424.
453 doi:10.1111/j.1365-246X.2005.02579.x.
- 454 Anderson, T.L., 2017. *Fracture mechanics: fundamentals and applications*.
455 CRC press.
- 456 Bar-sinai, Y., Spatschek, R., Brener, E.a., Bouchbinder, E., 2014. On the
457 velocity-strengthening behavior of dry friction. *Journal of Geophysical*
458 *Research* 119, 1738–1748. doi:10.1002/2013JB010586.Abstract.
- 459 Barras, F., Aldam, M., Roch, T., Brener, E.A., Bouchbinder, E., Molinari,
460 J.F., 2020. The Emergence of Crack-like Behavior of Frictional Rupture:
461 Edge Singularity and Energy Balance. *Earth and Planetary Science Letters*
462 531, 115978. doi:10.1016/j.epsl.2019.115978.
- 463 Bayart, E., Svetlizky, I., Fineberg, J., 2016. Fracture mechanics determine
464 the lengths of interface ruptures that mediate frictional motion. *Nature*
465 *Physics* 12, 166–170. doi:10.1038/nphys3539.
- 466 Brantut, N., 2020. Dilatancy-induced fluid pressure drop during
467 dynamic rupture: Direct experimental evidence and consequences
468 for earthquake dynamics. *Earth and Planetary Science Letters*
469 538, 116179. URL: <https://doi.org/10.1016/j.epsl.2020.116179>,
470 doi:10.1016/j.epsl.2020.116179, arXiv:1904.10906.
- 471 Brantut, N., Viesca, R.C., 2017. The fracture energy of ruptures

472 driven by flash heating. *Geophysical Research Letters* 44, 6718–6725.
473 doi:10.1002/2017GL074110.

474 Brener, E., Bouchbinder, E., 2021a. Theory of unconventional singularities
475 of frictional shear cracks. *Journal of the Mechanics and Physics of Solids*
476 153, 104466. doi:10.1016/j.jmps.2021.104466.

477 Brener, E., Bouchbinder, E., 2021b. Unconventional singularities and en-
478 ergy balance in frictional rupture. *Nature Communications* 12, 2585.
479 doi:10.1038/s41467-021-22806-9.

480 Brener, E.A., Marchenko, V.I., 2002. Frictional shear cracks. *JETP Letters*
481 76, 211–214. doi:10.1134/1.1517386, arXiv:0204046.

482 Chen, X., Chitta, S.S., Zu, X., Reches, Z., 2021. Dynamic fault weakening
483 during earthquakes: Rupture or friction? *Earth and Planetary Science*
484 *Letters* 575, 117165.

485 Di Toro, G., Han, R., Hirose, T., De Paola, N., Nielsen, S., Mi-
486 zoguchi, K., Ferri, F., Cocco, M., Shimamoto, T., 2011. Fault
487 lubrication during earthquakes. *Nature* 471, 494–499. URL:
488 <http://dx.doi.org/10.1038/nature09838>, doi:10.1038/nature09838.

489 Freund, L.B., 1979. The mechanics of dynamic shear crack propaga-
490 tion. *Journal of Geophysical Research: Solid Earth* 84, 2199–2209.
491 doi:10.1029/JB084iB05p02199.

492 Freund, L.B., 1998. *Dynamic fracture mechanics*. Cambridge university
493 press.

- 494 Garagash, D.I., Detournay, E., Adachi, J.I., 2011. Multiscale tip asymptotics
495 in hydraulic fracture with leak-off. *Journal of Fluid Mechanics* 669, 260–
496 297. doi:10.1017/S002211201000501X.
- 497 Goldsby, D., Tullis, T., 2011. Flash Heating Leads to Low Frictional Earth-
498 quake Slip Rates. *Science* 334, 216–218.
- 499 Hirose, T., Shimamoto, T., 2005. Growth of molten zone as a mecha-
500 nism of slip weakening of simulated faults in gabbro during frictional
501 melting. *Journal of Geophysical Research: Solid Earth* 110, 1–18.
502 doi:10.1029/2004JB003207.
- 503 Kammer, D.S., McLaskey, G.C., 2019. Fracture energy estimates from large-
504 scale laboratory earthquakes. *Earth and Planetary Science Letters* 511,
505 36–43. doi:10.1016/j.epsl.2019.01.031.
- 506 Kammer, D.S., Radiguet, M., Ampuero, J.P., Molinari, J.F., 2015. Lin-
507 ear elastic fracture mechanics predicts the propagation distance of
508 frictional slip. *Tribology Letters* 57. doi:10.1007/s11249-014-0451-8,
509 [arXiv:1408.4413](https://arxiv.org/abs/1408.4413).
- 510 Lambert, V., Lapusta, N., 2020. Rupture-dependent breakdown energy in
511 fault models with thermo-hydro-mechanical processes. *Solid Earth* 11,
512 2283–2302. doi:10.5194/se-11-2283-2020.
- 513 Marone, C., 1998. Laboratory-derived friction laws and their application
514 to seismic faulting. *Annual Review of Earth and Planetary Sciences* 26,
515 643–696. doi:10.1146/annurev.earth.26.1.643.

- 516 Marshall, G., Coutts, L.H., Williams, J., 1974. Temperature effects in the
517 fracture of pmma. *Journal of Materials Science* 9, 1409–1419.
- 518 Molinari, A., Estrin, Y., Mercier, S., 1999. Dependence of the coefficient of
519 friction on the sliding conditions in the high velocity range. *Journal of*
520 *Tribology* 121, 35–41. doi:10.1115/1.2833808.
- 521 Paglialunga, F., Passelègue, F., Brantut, N., Barras, F., Lebihain, M., Violay,
522 M., 2022. On the scale dependence in the dynamics of frictional rupture
523 : Constant fracture energy versus size-dependent breakdown work. *Earth*
524 *and Planetary Science Letters* 584. doi:10.1016/j.epsl.2022.117442.
- 525 Palmer, A.C., Rice, J.R., 1973. The growth of slip surfaces in the pro-
526 gressive failure of over-consolidated clay. *Royal society* 548, 527–548.
527 doi:10.1098/rspa.1973.0040.
- 528 Reches, Z., Lockner, D.A., 2010. Fault weakening and earthquake instability
529 by powder lubrication. *Nature* 467, 452–455. doi:10.1038/nature09348.
- 530 Rice, J.R., 1980. The mechanics of earthquake rup-
531 ture. *Physics of the Earth's Interior* , 555–649URL:
532 <http://citeseerx.ist.psu.edu/viewdoc/summary?doi=10.1.1.161.3251>,
533 doi:10.1.1.161.3251.
- 534 Rice, J.R., 2006. Heating and weakening of faults during earth-
535 quake slip. *Journal of Geophysical Research: Solid Earth* 111, 1–29.
536 doi:10.1029/2005JB004006.
- 537 Rice, J.R., Rudnicki, J.W., 1979. Earthquake precursory effects due to pore

- 538 fluid stabilization of a weakening fault zone. *Journal of Geophysical Re-*
539 *search: Solid Earth* 84, 2177–2193. doi:10.1029/JB084iB05p02177.
- 540 Rosakis, A.J., Rubino, V., Lapusta, N., 2020. Recent Milestones in Un-
541 raveling the Full-Field Structure of Dynamic Shear Cracks and Fault
542 Ruptures in Real-Time : From Photoelasticity to Ultrahigh- Speed
543 Digital Image Correlation. *Journal of Applied Mechanics* 87, 030801.
544 doi:10.1115/1.4045715.
- 545 Rubino, V., Rosakis, A.J., Lapusta, N., 2017. Understanding dynamic fric-
546 tion through spontaneously evolving laboratory earthquakes. *Nature Com-*
547 *munications* 8. doi:10.1038/ncomms15991.
- 548 Segall, P., Rubin, A.M., Bradley, A.M., Rice, J.R., 2010. Dilatant strength-
549 ening as a mechanism for slow slip events. *Journal of Geophysical Research:*
550 *Solid Earth* 115, 1–37. doi:10.1029/2010JB007449.
- 551 Svetlizky, I., Fineberg, J., 2014. Classical shear cracks drive the onset of dry
552 frictional motion. *Nature* 509, 205–208. doi:10.1038/nature13202.
- 553 Tinti, E., Spudich, P., Cocco, M., 2005. Earthquake fracture energy inferred
554 from kinematic rupture models on extended faults. *Journal of Geophysical*
555 *Research: Solid Earth* 110, 1–25. doi:10.1029/2005JB003644.
- 556 Viesca, R.C., Garagash, D.I., 2015. Ubiquitous weakening of faults
557 due to thermal pressurization. *Nature Geoscience* 8, 875–879.
558 doi:10.1038/ngeo2554.
- 559 Xu, S., Fukuyama, E., Yamashita, F., 2019. Robust Estimation of Rupture

560 Properties at Propagating Front of Laboratory Earthquakes. Journal of
561 Geophysical Research 124, 766–788. doi:10.1029/2018JB016797.